


## Photoelectrocatalytic generation of miscellaneous oxygen-based radicals towards cooperative degradation of multiple organic pollutants in water

Yurou Zhou<sup>a</sup>, Guan Zhang <sup>a,\*</sup> and Jing Zou<sup>b</sup>

<sup>a</sup> School of Civil and Environmental Engineering, Harbin Institute of Technology, Shenzhen (HITSZ), China

<sup>b</sup> General Education Division, School of Humanities & Social Science, The Chinese University of Hong Kong, Shenzhen (CUHKSZ), China

\*Corresponding author. E-mail: zhangguan@hit.edu.cn

 GZ, 0000-0001-7089-7536

### ABSTRACT

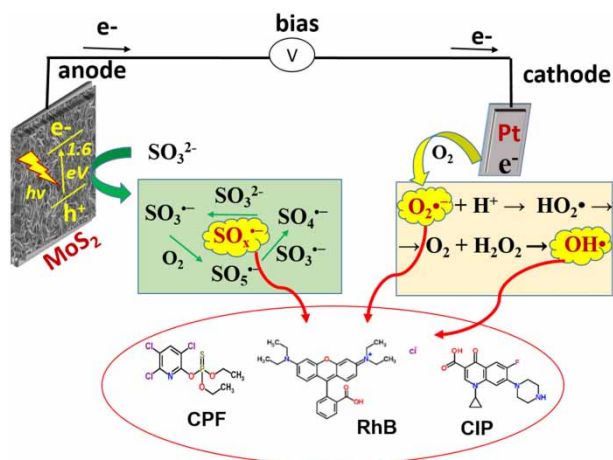
In the present photoelectrochemical (PEC) system utilizing MoS<sub>2</sub> nanoflakes as a wide spectrum absorptive photoanode, simultaneous PEC degradation of different organic pollutants was achieved by employing *in situ* generated oxysulfur radicals, superoxide and hydroxyl radicals as strong oxidants. In order to better understand the cooperative PEC degradation of representative organic pollutants including rhodamine B dye (RhB), chlorpyrifos (CPF) and ciprofloxacin (CIP), the influences by bias potential, solution pH, radical scavenger, dissolved oxygen concentration and electrolyte concentration have been investigated. The selective PEC degradation efficiency follows the order of CPF > RhB > CIP in mixed substrates condition. In addition, the degradation rate for the single substrate degradation was about two times higher compared to that in mixed substrates degradation. The experimental results verified that reactive oxidation species (ROS) including oxysulfur radicals, superoxide and hydroxyl radicals can be efficiently produced on both anode and cathode under visible light irradiation, and they work together for simultaneous degradation of different pollutants, but the contribution of each ROS for pollutant degradation is substrate dependent. These results indicate that cooperative oxidation of multiple pollutants by miscellaneous oxygen-based radicals should be further considered as a promising advanced oxidation technique.

**Key words:** advanced oxidation, cooperative oxidation, multiple radicals, organics degradation, photoelectrocatalysis

### HIGHLIGHTS

- MoS<sub>2</sub> nanoflakes on Ti sheet were prepared as a wide spectrum absorption anode.
- Sulfite ions served as electrolyte, precursor of oxysulfur radicals and hole scavenger.
- Multiple radical species can be produced by PEC activation of sulfite under visible light.
- Cooperative degradation of organic pollutants in wastewater was achieved.
- The contribution of each radical species for pollutant degradation was substrate-dependent.

## GRAPHICAL ABSTRACT



## INTRODUCTION

Advanced oxidation processes (AOPs), as pretreatment approaches to increase biodegradability of wastewater or secondary treatment approaches after biological water treatment to further reduce the amount of organic pollutants, are increasingly employed for treatment of different types of organic wastewater. In addition, recalcitrant, high toxic, persistent and new emerging pollutants with low concentrations in wastewater, such as endocrine disrupting chemicals (EDCs), pharmaceuticals and personal care products (PPCPs) and persistent organic pollutants (POPs), are hardly removed by traditional physiochemical or biochemical approaches (Zhang *et al.* 2015; Huang *et al.* 2017). The AOPs utilize radical species (mainly hydroxyl radical,  $\bullet\text{OH}$ ) as strong oxidants for mineralization of different types of pollutants. Among the different types of AOPs (ozone oxidation, electro-catalytic oxidation, photo(electro)catalytic oxidation, Fenton oxidation, wet oxidation etc.), and photoelectrocatalytic (PEC) degradation of water pollutants has been broadly studied as one of the promising oxidation techniques (Pawar *et al.* 2015; Wu *et al.* 2015; Xia *et al.* 2017a, 2017b). However, whether in the photocatalytic or photoelectrocatalytic process, the search for abundant, stable and efficient photocatalytic materials is especially crucial from the perspective of practical application (Zhao *et al.* 2013; Ji *et al.* 2017; Liu *et al.* 2017a, 2017b).

On the other hand, even though hydroxyl radical has strong oxidation potential (2.8 V vs. SHE), it is not omnipotent since some kinds of water pollutants are resistant to its oxidation. For example, ammonia nitrogen is hardly completely removed by hydroxyl radicals (Deng & Ezyzke 2011). Some research groups have reported conversion of ammonia nitrogen by photocatalysis, but most of the processes are less efficient (Wang *et al.* 2014; Bian *et al.* 2015; Dozzi *et al.* 2017; Liu *et al.* 2017a, 2017b). Our previous work also found that the molecular structures and properties of pollutants have a strong influence on the  $\bullet\text{OH}$  mediated PEC degradation efficiency with the degradation rate order of chlorpyrifos > rhodamine B > 4-chlorophenol > ciprofloxacin (Zhou *et al.* 2019). Varanasi *et al.* (2018) also proposed that  $\bullet\text{OH}$  selectively attack the aliphatic components, whereas  $\text{Cl}^{\bullet}$  induces transformation of olefinic species, and transformation of aromatic and olefinic moieties by  $\text{SO}_4^{\bullet-}$  are the predominant pathway for removal of dissolved organic matter in UV-AOPs. Thus, the AOPs relying on hydroxyl radical alone are not sufficient for the handling of multiple recalcitrant pollutants. Besides the conventional  $\bullet\text{OH}$  based AOPs, other radical species including superoxide radical ( $\text{O}_2^{\bullet-}$ ), chlorine radical ( $\text{Cl}^{\bullet}$ ), oxysulfur radicals ( $\text{SO}_3^{\bullet-}$ ,  $\text{SO}_4^{\bullet-}$  and  $\text{SO}_5^{\bullet-}$  radicals), persulfate radical ( $\text{S}_2\text{O}_8^{\bullet-}$ ) and their combination mediated newly emerging AOPs have been paid more attention recently (He *et al.* 2014; Lutze *et al.* 2015; Remucal & Manley 2016; Jasper *et al.* 2017; Xia *et al.* 2017a, 2017b; Zhu *et al.* 2020; Ji *et al.* 2021). For instance, electrochemical and photoelectrochemical oxidation of ammonia by  $\text{Cl}^{\bullet}$  have been reported as efficient approaches for complete removal of ammonia (Yang *et al.* 2016; Shin *et al.* 2017).  $\text{SO}_4^{\bullet-}$  radical in company with  $\text{Cl}^{\bullet}$  and  $\bullet\text{OH}$  radicals-based water treatment has been studied (Lutze *et al.* 2015). In addition, an expanding range of sulfite, sulfate or persulfates activation methods have been established to generate oxysulfur radicals for degradation of organic pollutants (Farhat *et al.* 2015; Hu & Long 2016; Chen *et al.* 2017; Zhi *et al.* 2017).

To address the problems of AOPs as mentioned above, we attempt to explore a new PEC oxidation system based on multiple oxygen based radical species. Specifically, oxysulfur radicals are generated *in situ* at the photoanode, and O<sub>2</sub> reduction generated radicals like O<sub>2</sub><sup>-</sup> and •OH are produced at the cathode. These oxidative radicals can realize simultaneous degradation of different types of wastewater pollutants. Herein, MoS<sub>2</sub> nanoflakes grown on Ti sheet as a wide spectrum absorption photoanode was employed since it has a strong visible light absorption capability (band gap ~1.5–1.8 eV) and suitable valence band position (1.3–1.5 V vs SHE) for oxidation of sulfite to generate sulfite radical (Liu *et al.* 2016). Upon the analytical, microscopic and spectroscopic characterization of prepared MoS<sub>2</sub> electrodes, the degradation of three organic pollutants (chlorpyrifos as a representative of pesticide, rhodamine B as a representative of dye and ciprofloxacin as a representative of pharmaceutical) either in single substrate condition or mixed substrates condition was tested. These organic pollutants may coexist in some kinds of wastewater or sewage streams in different concentration levels, therefore the PEC degradation of three pollutants in mixed systems was studied. Furthermore, another goal of this work is to explore the molecular structure related degradation behavior, as the three pollutants have different molecular structures. Importantly, we have demonstrated that the *in situ* generated oxysulfur radicals, superoxide and hydroxyl radicals are key oxidants for the simultaneous degradation of different organic pollutants.

## EXPERIMENTAL

### Preparation and characterization of MoS<sub>2</sub> photoanode

The as-prepared MoS<sub>2</sub> nanoflakes on Ti film (MoS<sub>2</sub>) and further annealed at 300 °C in reducing atmosphere (MoS<sub>2</sub>(300 °C)) were obtained by a hydrothermal method, and detailed information can be found in our previous work (Zhou *et al.* 2019). The morphology, microstructure and crystal phases of MoS<sub>2</sub>/Ti electrodes were characterized using a field emission scanning electron microscope (FESEM, SU8010), high resolution transmission electron microscope (HRTEM, Tecnai G2 F30), and X-ray diffraction (XRD, Bruker D8 Advance). Raman spectra of MoS<sub>2</sub> samples was measured with 532 nm excitation (LabRAMHR-800). Surface chemical composition and valence state of the samples were analysed by X-ray photoelectron spectroscopy (XPS, PHI 5000 VersaProbe II) with a monochromatic Al K $\alpha$  ray source. The band-gap energies of different MoS<sub>2</sub>/Ti films were measured by a UV-Vis spectrophotometer (JASCO V-7000).

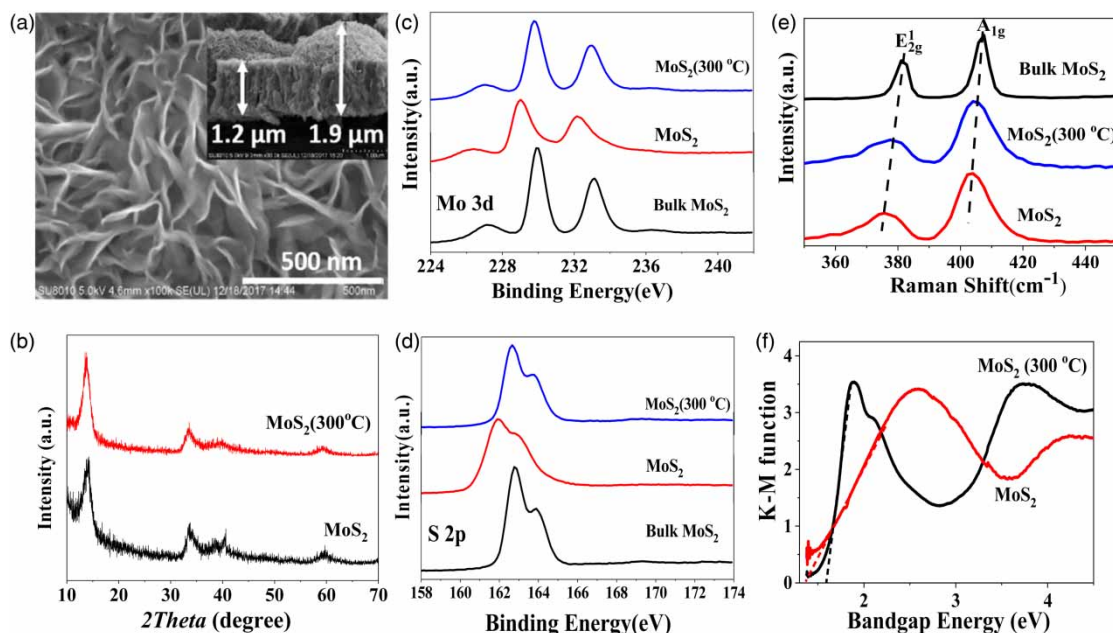
### Photoelectrochemical (PEC) performance evaluation

The PEC performance of different MoS<sub>2</sub> samples was tested by an electrochemical workstation (CHI660E, Shanghai Chenhua). Typically, the photocurrents of the MoS<sub>2</sub> photoanodes were recorded in 0.02 M Na<sub>2</sub>SO<sub>3</sub> electrolyte and 0.5 V bias under visible light irradiation ( $\geq 420$  nm) by a 300 W Xe arc lamp with a 420 nm filter (PLS-SXE300, light intensity 95.5 mW/cm<sup>2</sup>) according to our previous optimization study (Zhou *et al.* 2019). The PEC degradation of rhodamine B (RhB) dye (2.0  $\mu$ mol/L) and chlorpyrifos (CPF) and ciprofloxacin (CIP) (10.0  $\mu$ mol/L) was carried out with applied bias of 0.3–0.5 V in 0.01–0.05 M Na<sub>2</sub>SO<sub>3</sub> electrolyte in the pH range of 3–11 utilizing an MoS<sub>2</sub>(300 °C) electrode (electrode area = 1.0 cm<sup>2</sup>). Continuous and slow air bubbling into the reactor aimed to provide higher amounts of oxygen for enhancing generation of radicals on the cathode and degradation efficiency. The concentration of RhB, CPF and CIP at different intervals was analysed by a UV-Visible spectrophotometer (Shimadzu UV-3600), gas chromatograph (GC, Fuli 9790) and high performance liquid chromatography (HPLC, Waters E2695). Detailed analytical information can be found in our previous work (Zhou *et al.* 2019). A series of radical trapping experiments were carried out by adding 5 vol.% methanol, tert-butyl alcohol (TBA) and 2,2,6,6-tetramethylpiperidine (TEMPO, 1 mM) as scavengers, respectively, in order to determine the role of each radical species.

## RESULTS AND DISCUSSION

### Physicochemical characterization of different MoS<sub>2</sub> electrodes

Figure 1(a) and Figure S1 (supplementary data) display the morphologies and microstructures of as-prepared MoS<sub>2</sub>/Ti electrode (MoS<sub>2</sub>) from hydrothermal synthesis and further annealed electrode at 300 °C (MoS<sub>2</sub>(300 °C)). The vertically grown MoS<sub>2</sub> nanoflakes with a thickness of *ca.* 4–10 nm standing on Ti substrate were obtained by hydrothermal synthesis as shown in the SEM images. However, there are more cracks on the further annealed MoS<sub>2</sub> sample at 300 °C (Figure S1), probably because of the shrinkage and further growth of MoS<sub>2</sub>, whereas the thickness of MoS<sub>2</sub> was not markedly varied. The length of vertically aligned MoS<sub>2</sub> layer on Ti substrate is about 1.2–2.0  $\mu$ m for MoS<sub>2</sub> and MoS<sub>2</sub>(300 °C) from the SEM image cross-section view,



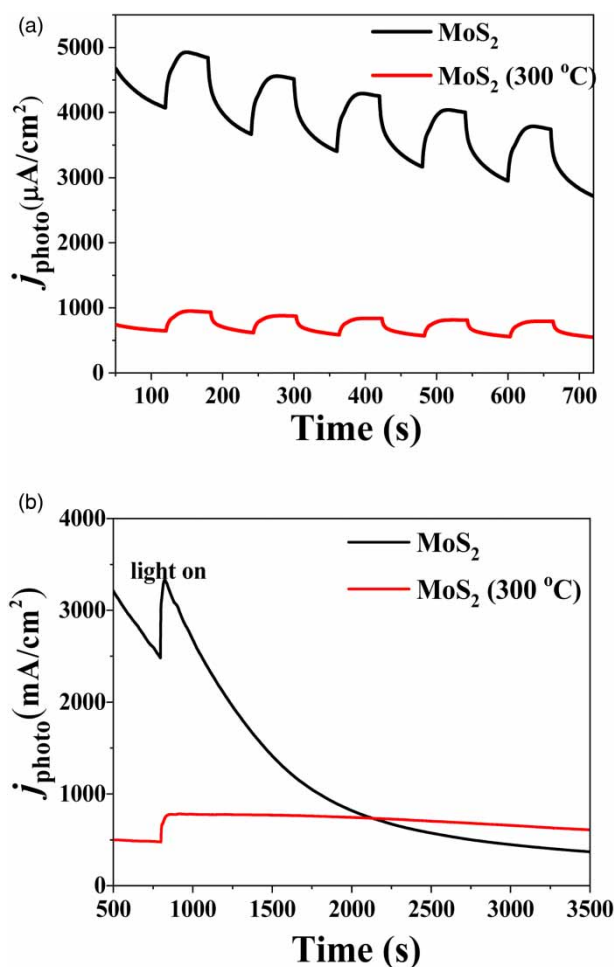
**Figure 1** | (a) Top view and cross-section (inset) SEM images of MoS<sub>2</sub>(300 °C) nanoflakes photoanode; (b) XRD patterns of different MoS<sub>2</sub> photoanodes; (c) Mo 3d XPS spectra of different MoS<sub>2</sub> photoanode; (d) S 2p XPS spectra of different MoS<sub>2</sub> photoanodes; (e) Raman spectra of different MoS<sub>2</sub> photoanodes; (f) Diffused reflectance spectra of different MoS<sub>2</sub> photoanodes with K–M function plot.

as shown in the inset of Figure 1(a). In addition, the layered crystalline structure of MoS<sub>2</sub> can be identified from the HR-TEM images and SAED patterns (see Figure S2). The XRD patterns of different MoS<sub>2</sub> samples are shown in Figure 1(b). In reference to the standard MoS<sub>2</sub> diffraction peaks (JCPDS card: 73–1508), broad diffraction peaks at 14.4 and 34.1° with relatively low intensities are clearly exhibited for the MoS<sub>2</sub> sample. The MoS<sub>2</sub>(300 °C) sample presents a higher diffraction peak of the (002) plane at 14.4° due to the enhanced crystallinity of MoS<sub>2</sub> nanoflakes after annealing at higher temperature.

Surface elemental XPS analysis of two prepared MoS<sub>2</sub> samples along with a commercial bulk MoS<sub>2</sub> sample (shown in Figure 1(c) and 1(d)) reflects some structural difference between the two prepared MoS<sub>2</sub> samples. The two peaks centered at ca. 230 and 233 eV (Mo 3d<sub>5/2</sub> and Mo 3d<sub>3/2</sub>) for the bulk MoS<sub>2</sub> and MoS<sub>2</sub>(300 °C) samples, and appeared at relatively higher binding energies compared to those of the as-prepared MoS<sub>2</sub> sample. Meanwhile, the S 2p doublet peaks for the bulk MoS<sub>2</sub> and MoS<sub>2</sub>(300 °C) samples located at 163–164 eV, which is relatively higher than that of the as-prepared MoS<sub>2</sub>. It was reported that Mo and S peaks of MoS<sub>2</sub> in 2H phase located at higher binding energy compared to 1T phase MoS<sub>2</sub>, indicating that structural transformation from 1T phase to stable 2H phase occurred during the post annealing treatment. The representative Raman peaks of different MoS<sub>2</sub> samples are shown in Figure 1(e). The Raman peaks located at 383 and 409 cm<sup>-1</sup> correspond to the in-plane (E<sub>2g</sub>) and out-of-plane (A<sub>1g</sub>) lattice vibrations. The Raman peaks of commercial bulk MoS<sub>2</sub> are narrow and sharp, whereas those for the prepared MoS<sub>2</sub> samples are broad, and there are slight Raman shifts for the prepared MoS<sub>2</sub> nanoflakes samples compared to the bulk MoS<sub>2</sub>, probably due to edge effect and increased electronic transition energies in few-layered MoS<sub>2</sub>. The band-gap energies of prepared MoS<sub>2</sub> film samples were evaluated by diffused reflection spectroscopy and the KM-plots of DRS spectra are shown in Figure 1(f). The band-gap energy of MoS<sub>2</sub> is associated with transitions from p-orbitals of the S atom to d-orbitals of the Mo atom in the visible light region (400–800 nm), and depends on physicochemical characters such as layer thickness and defects etc. The band-gap energies of the MoS<sub>2</sub> sample and MoS<sub>2</sub>(300 °C) sample are about 1.35 and 1.60 eV, respectively. The increased band-gap energy of the MoS<sub>2</sub>(300 °C) sample was probably due to the removal of intermediate defects, when the MoS<sub>2</sub> nanoflakes were annealed at higher temperature. The suitable band-gap energies of MoS<sub>2</sub> samples allow them to efficiently absorb solar light in a visible light region.

### Photoelectrochemical measurements

Figure 2(a) exhibits the photocurrent response (*i* – *t* curves) of different MoS<sub>2</sub> films under visible light irradiation at biased potentials of 0.5 V in 0.02 M Na<sub>2</sub>SO<sub>3</sub> electrolyte. The photocurrent of MoS<sub>2</sub> was slightly reduced for the sample after




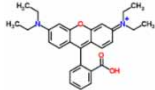
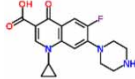
**Figure 2** | (a) Chopped photocurrent–time ( $i-t$ ) curves and (b) continuous photocurrent–time ( $i-t$ ) curves of different MoS<sub>2</sub> photoanodes under 0.5 V bias (vs. Ag/AgCl) in 0.02 M Na<sub>2</sub>SO<sub>3</sub> electrolyte.

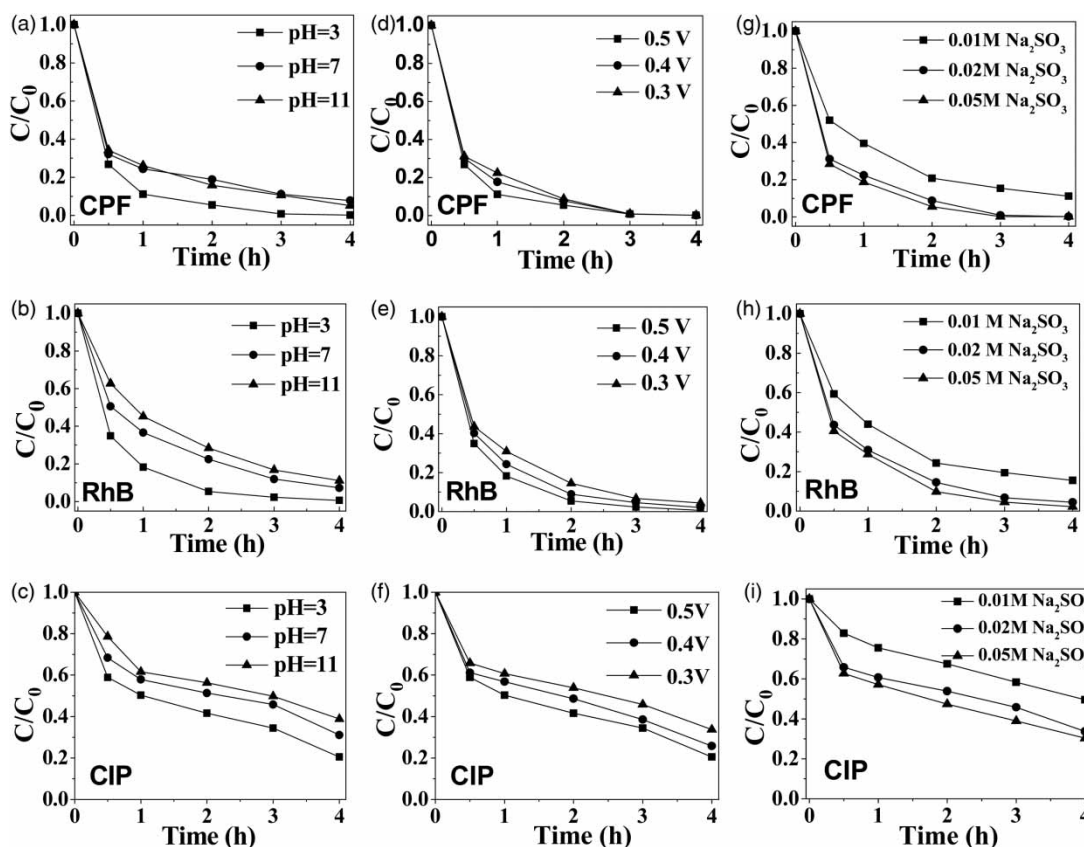
annealing MoS<sub>2</sub> (300 °C). It was also found that the generated photocurrents are slowly increased and decreased during the cycled light ‘on-off’ processes. This slow photoresponse may be attributed to several aspects such as weak interfacial connection between Ti substrate and MoS<sub>2</sub> nanoflakes, intrinsic defects within MoS<sub>2</sub>, and fast recombination of photogenerated charge carriers as evidenced from the physiochemical characterization. Furthermore, in the continuous test condition (Figure 2(b)), the as-prepared MoS<sub>2</sub> sample is extremely unstable, whereas the MoS<sub>2</sub>(300 °C) sample is relatively more stable for the generation of photocurrents due to the post thermal treatment. Thus, the MoS<sub>2</sub>(300 °C) sample was further selected for testing the PEC degradation of pollutants.

Three kinds of organic pollutants including rhodamine B dye (RhB), chlorpyrifos (CPF) and ciprofloxacin (CIP) (as shown in Table 1) were selected as representative pollutants in wastewater. Both a single substrate degradation experiment and mixed substrates degradation experiment were performed to investigate the selective degradation behavior of the MoS<sub>2</sub>(300 °C) sample. The experimental parameters such as pH, bias potential, and electrolyte concentration were first studied for the degradation of mixed substrates, and the results are shown in Figure 3. The PEC degradation of three substrates was more favored in acidic conditions, as the PEC degradation rates were gradually increased when decreasing the solution pH from 11 to 3. Reducing the bias potential from 0.5 to 0.3 V does not markedly reduce the PEC degradation of the three substrates. However, increasing the electrolyte concentration from 0.01 to 0.05 M gradually improves the PEC degradation rate. From an energy and cost consumption point of view, the optimized PEC degradation condition was screened out with 0.3 V bias, pH 3 and 0.02 M Na<sub>2</sub>SO<sub>3</sub>. Under such optimized conditions, substrate-dependent degradation behavior can be clearly observed. The PEC degradation efficiency follows the order of CPF > RhB > CIP, as shown in Figure 4(a). The PEC

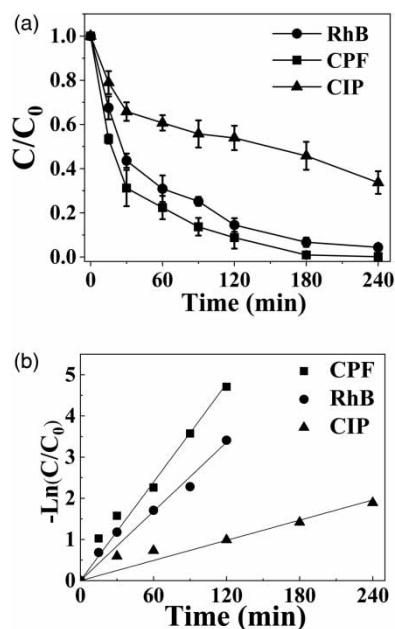


**Table 1** | Molecular structures and degradation rate constants ( $k$ ) at pH 3 during test conditions of single and mixed pollutants

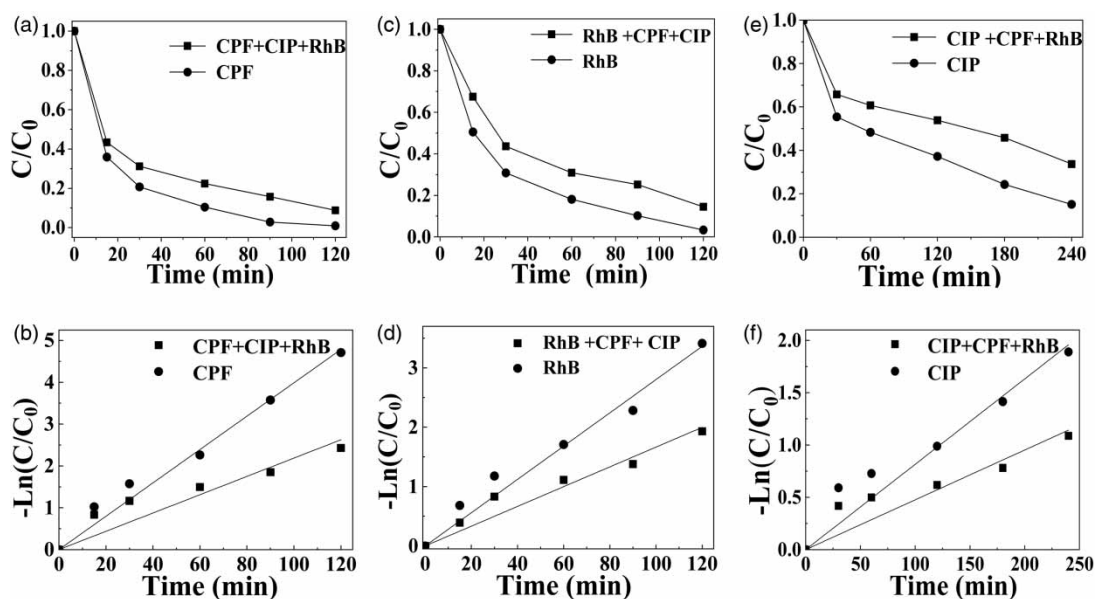
Pollutant	Structure	Single pollutant		Mixed pollutants	
		Rate $k$ ( $\text{min}^{-1}$ )	$R^2$	Rate $k$ ( $\text{min}^{-1}$ )	$R^2$
Chlorpyrifos (CPF)		0.0369	0.98	0.0175	0.91
Rhodamine B (RhB)		0.0259	0.97	0.0147	0.95
Ciprofloxacin (CIP)		0.007	0.95	0.0037	0.88

**Figure 3** | (a)–(c) pH effect; (d)–(f) applied bias potential effect; and (g)–(i) electrolyte concentration effect on the photoelectrochemical degradation of rhodamine B dye (RhB), chlorpyrifos (CPF) and ciprofloxacin (CIP). Under varied experimental conditions: pH = 3–11, 0.3–0.5 V bias (vs. Ag/AgCl) and 0.01–0.05 M  $\text{Na}_2\text{SO}_3$  electrolyte,  $[\text{RhB}] = 2 \mu\text{mol/L}$ ,  $[\text{CPF}] = [\text{CIP}] = 10 \mu\text{mol/L}$ .

degradation rate constant of CPF was approximately five times higher than that of CIP (Figure 4(b) and Table 1), implying that CIP is a more chemically stable compound. In addition, a single substrate degradation experiment was performed and its degradation profile was compared with the mixed substrate condition (Figure 5). Generally, the degradation rate for the single substrate degradation was about two times higher compared to that of mixed substrates degradation (shown in Table 1). This is reasonable since there would be more radical species attacking pollutants in the single substrate condition. On the other hand, there would be more pollutants subjected to oxidation in the presence of mixed pollutants compared to



**Figure 4** | (a) Profiles photoelectrochemical degradation of mixed three pollutants under optimized experimental conditions: pH = 3, 0.3 V bias (vs. Ag/AgCl) and 0.02 M Na<sub>2</sub>SO<sub>3</sub> electrolyte; (b) comparison of first-order kinetic curves of photoelectrochemical degradation of mixed pollutants.



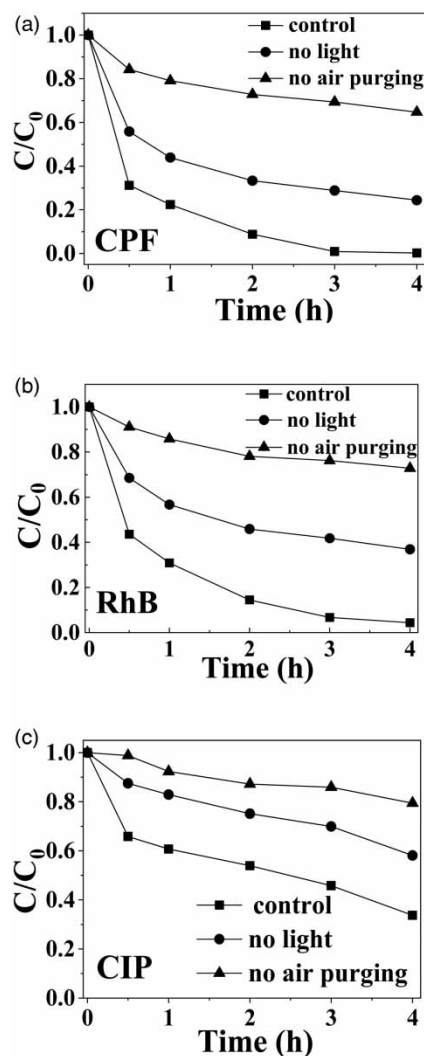
**Figure 5** | (a) and (b) Chlorpyrifos (CPF) degradation profiles and first-order kinetic curves in test of single pollutant and mixed pollutants conditions; (c) and (d) Rhodamine B (RhB) degradation profiles and first-order kinetic curves in test of single pollutant and mixed pollutants conditions; (e) and (f) ciprofloxacin (CIP) degradation profiles and first-order kinetic curves in test of single pollutant and mixed pollutants conditions. Experimental conditions: pH = 3, 0.3 V bias (vs. Ag/AgCl) and 0.02 M Na<sub>2</sub>SO<sub>3</sub> electrolyte.

that in the single pollutant conditions, because the recombination of generated oxidative radical species could be inhibited. In order to test the stability of the photoanode, multicycle experiments of RhB degradation were performed. As shown in Figure S3, after five cycle tests only slight PEC activity decay was observed, indicating the stability of the MoS<sub>2</sub>(300 °C) sample. The stable characters of the MoS<sub>2</sub>(300 °C) photoanode was attributed to the use of an Na<sub>2</sub>SO<sub>3</sub> electrolyte that can consume photo-generated holes on MoS<sub>2</sub> to prevent self-corrosion.

### Mechanism of PEC degradation of pollutants

The generation of reactive oxidative species (ROS) including  $\cdot\text{OH}$ ,  $\text{O}_2^{\cdot-}$ , and  $\text{H}_2\text{O}_2$  on cathode and oxysulfur radicals ( $\text{SO}_3^{\cdot-}$ ,  $\text{SO}_4^{\cdot-}$  and  $\text{SO}_5^{\cdot-}$ ) on the anode has been demonstrated in our previous work (Fan *et al.* 2019; Zhou *et al.* 2019). On the anode, the valence band potential (1.3–1.5 V *vs.* SHE) of  $\text{MoS}_2$  is not sufficient for oxidizing water to generate  $\cdot\text{OH}$  radicals, thus the self-oxidation of  $\text{S}^{2-}$  on the anode would be possible without hole scavengers. However, in the presence of sulfite electrolyte, the valence band holes generated on the nanostructured  $\text{MoS}_2$  film under visible light irradiation are able to oxidize sulfite to sulfite radicals, because the redox potential of  $\text{SO}_3^{\cdot-}/\text{SO}_3^{2-}$  couple is 1.2 V *vs.* SHE (Fan *et al.* 2019). Under such a setting, the self-oxidation of  $\text{MoS}_2$  electrode was significantly inhibited. On the other hand, the  $\text{SO}_3^{2-}$  could also be electrochemically oxidized under biased conditions to produce  $\text{SO}_3^{\cdot-}$ . On the cathode, both the photochemically and electrochemically generated electrons would reduce  $\text{O}_2$  to generate oxidative species like  $\text{O}_2^{\cdot-}$ ,  $\text{H}_2\text{O}_2$  and  $\cdot\text{OH}$ . To inhibit the side reactions of  $\text{H}_2$  production and enhance the generation of ROS, the reactor was continuously purged with air to feed higher amounts of oxygen. The oxygen effect on the degradation of pollutants can be seen in Figure 6. Without continuous air purging, only slight degradation of pollutants occurred for all the cases, probably because the dissolved oxygen was gradually depleted. This indicates that oxygen reduction-related ROS dominates the organics degradation.

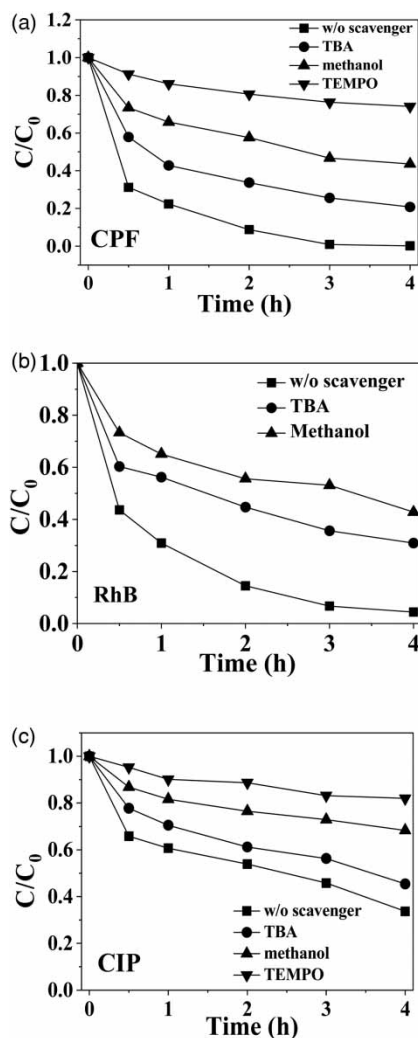
To further prove the relative contributions of ROS taking part in the degradation of pollutants, quenching tests were carried out by adding different radical scavengers (methanol, tert-butyl alcohol (TBA), and TEMPO). TEMPO is a good scavenger of



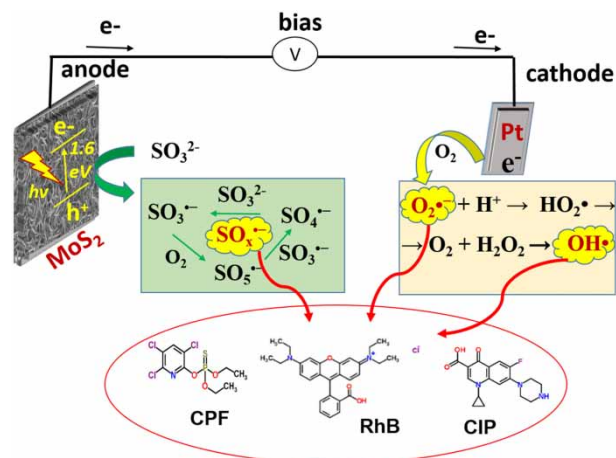
**Figure 6** | Photoillumination effect and dissolved oxygen concentration effects on the photoelectrochemical degradation of three pollutants (a) CPF; (b) RhB; (c) CIP. Experimental conditions: pH = 3, 0.3 V bias (*vs.* Ag/AgCl) and 0.02 M  $\text{Na}_2\text{SO}_3$  electrolyte.



radical species, methanol with an  $\alpha$ -H can effectively quench oxysulfur radicals (e.g.  $\text{SO}_4^{\cdot-}$ , second-order rate constant  $1.1 \times 10^7 \text{ Lmol}^{-1} \text{ s}^{-1}$ ),  $\cdot\text{OH}$  (second-order rate constant  $9.1 \times 10^8 \text{ Lmol}^{-1} \text{ s}^{-1}$ ) and holes, whereas TBA without an  $\alpha$ -H mainly reacts with  $\cdot\text{OH}$  (second-order rate constant  $6 \times 10^8 \text{ Lmol}^{-1} \text{ s}^{-1}$ ) and is not effective for oxysulfur radicals (e.g.  $\text{SO}_4^{\cdot-}$ ,  $4 \times 10^5 \text{ Lmol}^{-1} \text{ s}^{-1}$ ). According to the different scavenging effects, the key ROS to each pollutant can be inferred. As shown in Figure 7(a), the scavenging effect from high to low in the CPF degradation according to the reaction rate is TEMPO (for  $\cdot\text{OH}$ ,  $\text{SO}_x^{\cdot-}$ , and  $\text{O}_2^{\cdot-}$ ) > methanol (for  $\cdot\text{OH}$ ,  $\text{SO}_x^{\cdot-}$ ) > TBA (for  $\cdot\text{OH}$ ). This result is consistent with the fact that oxygen reduction-related ROS played a critical role in the degradation of pollutants. The holes may be effectively scavenged by the sulfite electrolyte, thus the difference of methanol and TBA scavenging may be attributed to the  $\text{SO}_x^{\cdot-}$  effect. For the RhB degradation test (Figure 7(b)), the TEMPO scavenging effect was excluded since its yellowish color has interference on the U-vis absorption of RhB solution. It can be seen that both methanol and TBA can effectively inhibit RhB degradation, indicating that  $\cdot\text{OH}$  and  $\text{SO}_x^{\cdot-}$  play a critical role in the RhB degradation. According to the scavenging effect,  $\cdot\text{OH}$  could be the main ROS for RhB degradation. In the case of CIP degradation (Figure 7(c)), TEMPO and methanol present more significant scavenging effects compared to TBA, implying that  $\text{SO}_x^{\cdot-}$  and  $\text{O}_2^{\cdot-}$  radicals could be the key ROS for its degradation. Previously, we also found that  $\cdot\text{OH}$  could not effectively degrade CIP, and Wang *et al.* (2018) reported that  $\text{O}_2^{\cdot-}$  and photohole ( $\text{h}^+$ ) from the  $\text{C}_3\text{N}_4$  photocatalyst are the main oxidants for CIP degradation. The scavenging experiments prove that all the ROS, including  $\cdot\text{OH}$ ,  $\text{O}_2^{\cdot-}$  and  $\text{SO}_x^{\cdot-}$ , participate in the organic degradation, as shown in Figure 8, but



**Figure 7** | Photoelectrochemical degradation of three pollutants: (a) chlorpyrifos (CPF); (b) rhodamine B dye (RhB); and (c) ciprofloxacin (CIP) in the presence of 5 vol.% tert-butyl alcohol (TBA), methanol and TEMPO (1 mM) as ROS scavengers.



**Figure 8** | Illustration of photoelectrochemical activation of sulfite for *in situ* generation of oxysulfur, superoxide and hydroxyl radicals towards simultaneous degradation of different pollutants.

the contribution of each ROS is substrate-dependent. However, oxygen reduction-related ROS generally contributes most to the pollutant degradation. The different oxidation characteristics of each ROS determine that they will preferentially attack different sites of pollutant molecules, and the degradation pathways and intermediates would be varied, which merits further study.

## CONCLUSIONS

In summary, an efficient  $\text{MoS}_2\text{-SO}_3^{2-}$  based AOP employing oxysulfur radicals, hydroxyl and superoxide radicals together for the degradation of different structured pollutants has been clearly demonstrated. The coexisting radicals allowed more efficient PEC degradation of multiple organic pollutants with different structures. The PEC degradation rates were affected by many parameters such as applied bias, solution pH, dissolved oxygen concentration, and properties of the pollutants. Generally, acidic pH conditions and higher electrolyte concentrations were more favored for pollutants degradation. The PEC degradation efficiency was also substrate-dependent, with the general degradation rate order of chlorpyrifos > rhodamine B > ciprofloxacin in both single and mixed substrates conditions.

## ACKNOWLEDGEMENTS

The authors are grateful for the financial support from NSFC (no. 51978197) and the Shenzhen Science and Technology Innovation Commission (Grant No. JCYJ20190813171403664), Basic research program of Guangdong Province (No. 2018A030313851).

## DATA AVAILABILITY STATEMENT

All relevant data are included in the paper or its Supplementary Information.

## REFERENCES

- Bian, Z., Cao, F., Zhu, J. & Li, H. 2015 Plant uptake-assisted round-the-clock photocatalysis for complete purification of aquaculture wastewater using sunlight. *Environ. Sci. Technol.* **49**, 2418–2424.
- Chen, L., Tang, M., Chen, C., Chen, M., Luo, K., Xu, J., Zhou, D. & Wu, F. 2017 Efficient bacterial inactivation by transition metal catalyzed auto-oxidation of sulfite. *Environ. Sci. Technol.* **51**, 12663–12671.
- Deng, Y. & Ezyske, C. M. 2011 Sulfate radical-advanced oxidation process (SR-AOP) for simultaneous removal of refractory organic contaminants and ammonia in landfill leachate. *Water Res.* **45**, 6189–6194.
- Dozzi, M. V., Brocato, S., Marra, G., Tozzola, G., Meda, L. & Selli, E. 2017 Aqueous ammonia abatement on Pt- and Ru-modified  $\text{TiO}_2$ : selectivity effects of the metal nanoparticles deposition method. *Catal. Today* **287**, 148–154.
- Fan, X., Zhou, Y., Zhang, G., Liu, T. & Dong, W. 2019 *In situ* photoelectrochemical activation of sulfite by  $\text{MoS}_2$  photoanode for enhanced removal of ammonium nitrogen from wastewater. *Appl. Catal. B Environ.* **244**, 396–406.

- Farhat, A., Keller, J., Tait, S. & Radjenovic, J. 2015 Removal of persistent organic contaminants by electrochemically activated sulfate. *Environ. Sci. Technol.* **49**, 14326–14333.
- He, X., Cruz, A., O'Shea, K. E. & Dionysiou, D. D. 2014 Kinetics and mechanisms of cytolindolol B destruction by sulfate radical-based advanced oxidation processes. *Water Res.* **63**, 168–178.
- Hu, P. & Long, M. 2016 Cobalt-catalyzed sulfate radical-based advanced oxidation: a review on heterogeneous catalysts and applications. *Appl. Catal. B Environ.* **181**, 103–117.
- Huang, N., Wang, T., Wang, W. L., Wu, Q. Y., Li, A. & Hu, H. Y. 2017 UV/chlorine as an advanced oxidation process for the degradation of benzalkonium chloride: synergistic effect, transformation products and toxicity evaluation. *Water Res.* **114**, 246–253.
- Jasper, J. T., Yang, Y. & Hoffmann, M. R. 2017 Toxic byproduct formation during electrochemical treatment of latrine wastewater. *Environ. Sci. Technol.* **51**, 7111–7119.
- Ji, Y., Bai, J., Li, L., Xia, L., Chen, S. & Zhou, B. 2017 Improved photoelectrocatalytic activities of BiOCl with high stability for water oxidation and MO degradation by coupling RGO and modifying phosphate groups to prolong carrier lifetime. *Water Res.* **125**, 512–519.
- Ji, J., Yan, Q., Yin, P., Mine, S., Matsuoka, M. & Xing, M. 2021 Defects on  $\text{CoS}_2-x$ : tuning redox reactions for sustainable degradation of organic pollutants. *Angew. Chem. Int. Ed.* **60**, 2903–2908.
- Liu, C., Kong, D., Hsu, P., Yuan, H., Lee, H., Liu, Y., Wang, H., Wang, S., Yan, K., Lin, D., Maraccini, P. A., Parker, K. M., Boehm, A. B. & Cui, Y. 2016 Rapid water disinfection using vertically aligned  $\text{MoS}_2$  nanofilms and visible light. *Nature Nanotech.* **11**, 1098–1105.
- Liu, S. Q., Zhu, X. L., Zhou, Y., Meng, Z. D., Chen, Z. G., Liu, C. B., Chen, F., Wu, Z. Y. & Qian, J. C. 2017a Smart photocatalytic removal of ammonia through molecular recognition of zinc ferrite reduced graphene oxide hybrid catalyst under visible light irradiation. *Catal. Sci. Technol.* **7**, 3210–3217.
- Liu, S., Zhao, X., Zeng, H., Wang, Y. & Qiao, M. 2017b Enhancement of photoelectrocatalytic degradation of diclofenac with persulfate activated by Cu cathode. *Chem. Eng. J.* **320**, 168–177.
- Lutze, H. V., Kerlin, N. & Schmidt, T. C. 2015 Sulfate radical-based water treatment in presence of chloride: formation of chlorate, interconversion of sulfate radicals into hydroxyl radicals and influence of bicarbonate. *Water Res.* **72**, 349–360.
- Pawar, R. C., Pyo, Y., Ahn, S. H. & Lee, C. S. 2015 Photoelectrochemical properties and photodegradation of organic pollutants using hematite hybrids modified by gold nanoparticles and graphitic carbon nitride. *Appl. Catal. B Environ.* **176–177**, 654–666.
- Remucal, C. K. & Manley, D. 2016 Emerging investigators series: the efficacy of chlorine photolysis as an advanced oxidation process for drinking water treatment. *Environ. Sci. Technol.* **2**, 565–579.
- Shin, Y. U., Yoo, H. Y., Kim, S., Chuang, K. M., Park, Y. G., Huang, K. H., Hong, S. W., Park, H., Cho, K. & Lee, J. 2017 Sequential combination of Electro-Fenton and electrochemical chlorination processes for the treatment of anaerobically-digested food wastewater. *Environ. Sci. Technol.* **51**, 10700–10710.
- Varanasi, L., Coscarelli, E., Khaksari, M., Mazzoleni, L. R. & Minakata, D. 2018 Transformations of dissolved organic matter induced by UV photolysis, hydroxyl radicals, chlorine radicals and sulfate radicals in aqueous-phase UV-Based advanced oxidation processes. *Water Res.* **135**, 22–30.
- Wang, H., Su, Y., Zhao, H., Yu, H., Chen, S., Zhang, Y. & Quan, X. 2014 Photocatalytic oxidation of aqueous ammonia using atomic single layer graphitic- $\text{C}_3\text{N}_4$ . *Environ. Sci. Technol.* **48**, 11984–11990.
- Wang, F., Feng, Y., Chen, P., Wang, Y., Su, Y., Zhang, Q., Zeng, Y., Xie, Z., Liu, H., Liu, Y., Lv, W. & Liu, G. 2018 Photocatalytic degradation of fluoroquinolone antibiotics using ordered mesoporous  $\text{g-C}_3\text{N}_4$  under simulated sunlight irradiation: kinetics, mechanism, and antibacterial activity elimination. *Appl. Catal. B Environ.* **227**, 114–122.
- Wu, Z., Zhao, G., Zhang, Y., Liu, J., Zhang, Y. N. & Shi, H. 2015 A solar-driven photocatalytic fuel cell with dual photoelectrode for simultaneous wastewater treatment and hydrogen production. *J. Mater. Chem. A* **3**, 3416–3424.
- Xia, D., Yin, R., Sun, J., An, T., Li, G., Wang, W., Zhao, H. & Wong, P. K. 2017a Natural magnetic pyrrhotite as a high-efficient persulfate activator for micropollutants degradation: radicals identification and toxicity evaluation. *J. Hazard. Mater.* **340**, 435–444.
- Xia, L. G., Bai, J., Li, J. H., Zeng, Q. Y., Li, L. S. & Zhou, B. X. 2017b High-performance  $\text{BiVO}_4$  photoanodes cocatalyzed with an ultrathin  $\alpha\text{-Fe}_2\text{O}_3$  layer for photoelectrochemical application. *Appl. Catal. B Environ.* **204**, 127–133.
- Yang, Y., Shin, J., Jasper, J. T. & Hoffmann, M. R. 2016 Multilayer heterojunction anodes for saline wastewater treatment: design strategies and reactive species generation mechanisms. *Environ. Sci. Technol.* **50**, 8780–8787.
- Zhang, G., Ni, C., Liu, L., Zhao, G., Fina, F. & Irvine, J. T. S. 2015 Macro-mesoporous resin as amorphous metal free visible light photocatalysts. *J. Mater. Chem. A* **3**, 15413–15419.
- Zhao, X., Guo, L., Zhang, B., Liu, H. & Qu, J. 2013 Photoelectrocatalytic oxidation of Cu–EDTA at the  $\text{TiO}_2$  electrode and simultaneous recovery of Cu by electrodeposition. *Environ. Sci. Technol.* **47**, 4480–4488.
- Zhi, Y., Bai, J., Li, J., Luo, T., Qiao, L., Zeng, Q. & Zhou, B. 2017 Highly selective transformation of ammonia nitrogen to  $\text{N}_2$  based on a novel solar-driven photoelectrocatalytic-chlorine radical reactions system. *Water Res.* **125**, 512–519.
- Zhou, Y., Fan, X., Zhang, G. & Dong, W. 2019 Fabricating  $\text{MoS}_2$  nanoflakes photoanode with unprecedented high photoelectrochemical performance and multi-pollutants degradation test for water treatment. *Chem. Eng. J.* **356**, 1003–1013.
- Zhu, L., Ji, J., Liu, J., Mine, S., Matsuoka, M., Zhang, J. & Xing, M. 2020 Designing 3D- $\text{MoS}_2$  sponge as excellent cocatalysts in advanced oxidation processes for pollutant control. *Angew. Chem. Int. Ed.* **59**, 13968–13976.